PHYSICS

Ultrastrong photon-to-magnon coupling in multilayered heterostructures involving superconducting coherence via ferromagnetic layers

Igor A. Golovchanskiy[1,2]*, Nikolay N. Abramov[2], Vasily S. Stolyarov[1,3], Martin Weides[4], Valery V. Ryazanov[2,5], Alexander A. Golubov[1,6], Alexey V. Ustinov[2,7,8], Mikhail Yu. Kupriyanov[1,9]

The critical step for future quantum industry demands realization of efficient information exchange between different-platform hybrid systems that can harvest advantages of distinct platforms. The major restraining factor for the progress in certain hybrids is weak coupling strength between the elemental particles. In particular, this restriction impedes a promising field of hybrid magnonics. In this work, we propose an approach for realization of on-chip hybrid magnonic systems with unprecedentedly strong coupling parameters. The approach is based on multilayered microstructures containing superconducting, insulating, and ferromagnetic layers with modified photon phase velocities and magnon eigenfrequencies. The enhanced coupling strength is provided by the radically reduced photon mode volume. Study of the microscopic mechanism of the photon-to-magnon coupling evidences formation of the long-range superconducting coherence via thick strong ferromagnetic layers in superconductor/ferromagnet/superconductor trilayer in the presence of magnetization precession. This discovery offers new opportunities in microwave superconducting spintronics for quantum technologies.

INTRODUCTION

The past decade has seen a remarkable progress in experimental quantum information sciences and in the development of various artificial quantum systems. Originally, experimental quantum physics was pioneered by quantum optics, which introduced us to basic concepts of quantum information processing (1). With the invention of superconducting qubits, quantum technologies started to evolve in the direction of solid-state microwave superconducting circuits (2), whipping up the quantum computer race.

The next critical step in quantum industry demands realization of efficient information exchange between different-platform quantum systems (3, 4) that can harvest advantages of distinct systems. A number of promising systems are based on coherent interaction of photons with mechanical oscillations (phonons) (5) or collective spin excitations (magnons) (6) in ferromagnetic media. The latter is of particular interest for application in hybrid magnonic–based quantum platforms (7–10) and offers opportunities for the development of novel quantum technologies such as magnon memory (11) or microwave-to-optical quantum transducers (12).

The major restraining factor for the progress in hybrid quantum magnonics is the fundamentally weak coupling parameter between photons and magnons. This restriction is traditionally circumvented by a radical increase of a number of spins in the cavity hybrid system (9, 13–18), as the coupling scales with the square root of the number of spins in the system. Yet, owing to poor single-spin coupling strength, dimensions of hybrid elements in cavity systems become macroscopic. A transition to the on-chip hybrid magnonics requires engineering of circuits with large local microwave fields and reduced microwave mode volume (19, 20). Tunability and control over losses in these miniaturized systems are not easy to achieve. Currently, with both approaches, the realization of scalable magnonic hybrids with freely adjustable coupling characteristics remains unattainable. The problem of inefficient photon-to-magnon coupling is also relevant in classical magnonic devices (21), which forces developments of alternative-to-microwave excitation/detection schemes (22) and also stimulates the development of alternative types of magnon-magnon hybrids (23, 24).

In this work, we demonstrate the realization of ultrastrong photon-to-magnon coupling with the following peak characteristics: coupling strength above 2 GHz, single-spin coupling strength about 90 Hz, cooperativity reaching 240, and coupling constant reaching 0.92 (or the coupling ratio reaching 0.43). The latter parameter indicates the operation of the hybrid system in the ultrastrong coupling regime of light-matter interaction where about 80% of the total energy in the system is swapped between the photons and magnons within a single oscillation period of the individual uncoupled resonators. These characteristics are achieved as a result of electromagnetic interaction between two subsystems: a superconductor/insulator/superconductor thin-film heterostructure, where the phase velocity of photons is substantially reduced, and a superconductor/ferromagnet/superconductor thin-film heterostructure, where superconducting proximity at both interfaces enhances the collective spin eigenfrequencies (25–27).

As it turned out, by addressing the photon-to-magnon coupling problem with our system, we have stumbled upon a new manifestation of superconducting spintronics (28, 29). Superconducting spintronics is based on the phenomenon of superconducting proximity in superconductor/ferromagnetic systems and considers the ability of a ferromagnet to carry the superconducting condensate. The latter is actually the challenge, owing to the antagonistic ordering of

[1]Moscow Institute of Physics and Technology, State University, 9 Institutskiy per., Dolgoprudny, Moscow Region 141700, Russia. [2]National University of Science and Technology MISIS, 4 Leninsky prosp., Moscow 119049, Russia. [3]Dukhov Research Institute of Automatics (VNIIA), Sushchevskaya 22, Moscow 127055, Russia. [4]James Watt School of Engineering, Electronics and Nanoscale Engineering Division, University of Glasgow, Glasgow G12 8QQ, UK. [5]Institute of Solid State Physics (ISSP RAS), Chernogolovka, Moscow Region 142432, Russia. [6]Faculty of Science and Technology and MESA+ Institute for Nanotechnology, University of Twente, 7500 AE Enschede, Netherlands. [7]Physikalisches Institut, Karlsruhe Institute of Technology, 76131 Karlsruhe, Germany. [8]Russian Quantum Center, Skolkovo, 143025 Moscow Region, Russia. [9]Skobeltsyn Institute of Nuclear Physics, MSU, Moscow 119991, Russia.
*Corresponding author. Email: golov4anskiy@gmail.com

spins by superconducting and ferromagnetic phenomena, and requires building systems with rather exotic ferromagnetic materials (30–32) or with technologically sophisticated ultrathin-film nanostructures (33, 34). In this work, we demonstrate the existence of superconducting coherence within superconductor/ferromagnet/superconductor trilayer that is accompanied by the magnetization precession. The large thickness of the ferromagnetic layer in comparison to typical superconducting-proximity coherence length scales suggests the spin-triplet origin of the coherence.

RESULTS AND DISCUSSION

A schematic illustration of investigated hybrid systems is shown in Fig. 1. The system consists of superconducting (S) niobium (Nb) film coplanar waveguide (CPW) and a series of multilayered rectangular-film heterostructures placed directly on top of the transmission line. Multilayered film heterostructures are fabricated with lateral dimensions $L \times W = 1100 \times 130\ \mu m^2$ out of Nb, ferromagnetic (F) permalloy (Py = $Fe_{20}Ni_{80}$), and insulating (I) Si or AlO_x layers. A number of different samples have been fabricated and measured with different thicknesses and orders of S, F, and I layers. The response of experimental samples was studied by analyzing the transmitted microwave signal $|S_{21}|(f, H)$ with the vector network analyzer (VNA) Rohde & Schwarz ZVB20 (see Materials and Methods for details).

Figure 2 collects experimental data for the PM1 sample that consist of I/S/F/S = Si (30 nm)/Nb (102 nm)/Py (35 nm)/Nb (103 nm) rectangles placed on top of 140-nm-thick Nb waveguide (see Table 1 and Fig. 1). Figure 2 (A to C) shows spectra $d|S_{21}|(f, H)/dH$ measured at $T = 2$ K (A) and $T = 7.5$ K (B), which are below the superconducting temperature of Nb $T_c \approx 9$ K, and at $T = 9.5$ K (C), which is slightly above the T_c. At $T > T_c$ (Fig. 2C), the spectrum consists of a single absorption line indicated as the F line. The F line represents the conventional ferromagnetic resonance (FMR) absorption by the F layer. The conventional FMR curve $f_r^F(H)$ for thin in-plane–magnetized ferromagnetic films at the in-plane magnetic field obeys the Kittel dependence

$$[2\pi f_r^F(H)/\mu_0\gamma]^2 = (H + H_a)(H + H_a + M_{eff})\qquad(1)$$

where f_r^F is the FMR frequency, μ_0 is the vacuum permeability, $\gamma = 1.856 \times 10^{11}$ red $(Ts)^{-1}$ is the gyromagnetic ratio for Py, H_a is the anisotropy field that is aligned with the external field, and M_{eff} is the effective magnetization. Modeling of the absorption line at $T > T_c$ with Eq. 1 yields negligible $\mu_0 H_a \sim 10^{-4}$ T and $\mu_0 M_{eff} = 1.13$ T, which are typical for Py thin films.

At $T < T_c$, the spectrum changes drastically. At $T = 2$ K (Fig. 2A), the spectrum contains three resonance lines indicated as the F line and S^+ and S^- lines. The roughly linear dependence of the absorption on the magnetic field (F line) corresponds to the FMR absorption by the hybrid S/F/S subsystem of the PM1 sample. As reported in (27), superconducting proximity in S/F/S trilayer modifies anisotropy fields, induces giant positive anisotropy H_a, and reduces the effective magnetization M_{eff}. These changes shift the FMR to higher frequencies.

S^+ and S^- lines in Fig. 2A are identified as the avoided crossing (also known as anti-crossing, level repulsion, or normal mode splitting) response (13, 14, 35) of two coupled oscillators: the ferromagnetic S/F/S resonator (F line) and a microwave photon resonator. The latter is characterized by the resonance frequency of about 17 GHz at zero field (frequency of the S^+ line at zero field). The microwave photon resonator is formed at the insulating layer of the PM1 sample between the Nb-CPW transmission line and the first S layer of the deposited I/S/F/S multilayer (see Fig. 1). In the insulating film constrained by two S layers, the photon phase velocity is reduced following the Swihart expression (36)

$$\bar{c} = c_0\sqrt{d_I/\varepsilon_I(2\lambda_L + d_I)}\qquad(2)$$

where c_0 is the velocity of light in vacuum, $\bar{c}$ is the modified velocity of light known as the Swihart velocity, d_I is the thickness of the I layer, ε_I is the dielectric constant of the I layer, and λ_L is the London penetration depth of the S layer. Considering $d_I = 30$ nm of the Si layer, $\varepsilon_I \approx 10$ for Si, and $\lambda_L \approx 90$ nm in Nb, one obtains $\bar{c} = 0.12\,c_0$ in the S/I/S subsystem of the PM1 sample, which provides the resonance frequency $f_r^S = \bar{c}/2L \approx 17$ GHz for a $\lambda/2$ resonator with the length of deposited rectangles $L = 1.1$ mm. This frequency exactly matches the resonance frequency of the microwave resonator at zero field in Fig. 2A. Therefore, S^+ and S^- lines correspond to the response of the coupled microwave S/I/S and ferromagnetic S/F/S resonators.

A more detailed understanding of the system can be obtained by analyzing the temperature dependence of the microwave transmission spectrum at $T < T_c$. Figure 2B shows the spectrum of the PM1 sample at $T = 7.5$ K$<T_c$. Visual comparison of Fig. 2 (A and B) shows that upon increasing temperature, the F line shifts to lower frequencies, which is consistent with the temperature dependence of the FMR in the S/F/S systems (27). Both S^+ and S^- lines also shift to lower frequencies. For instance, the zero-field frequency of the Swihart resonator shifts down to about 14 GHz (see S^+ line at zero field). This temperature dependence of the Swihart resonance is provided by the temperature dependence of the London penetration depth $f_r^S \propto 1/\sqrt{\lambda_L}$ (see Eq. 2). Also, Fig. 2B shows that the resonance frequency given by the S^- line decreases upon increasing magnetic field at $\mu_0 H > 120$ mT. The field dependence of the Swihart resonance frequency is provided by the field dependence of the London penetration depth of the s-wave superconductors $\lambda_L \propto H^2$ (37) and also by the dependence of the effective penetration depth
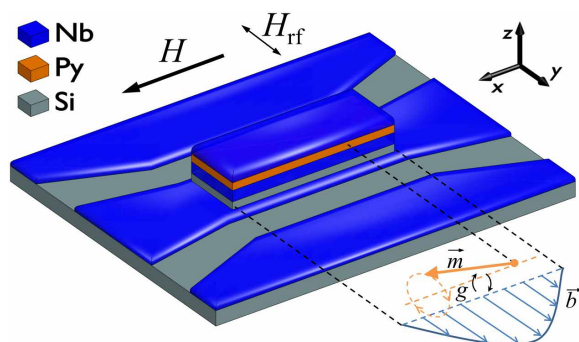

Fig. 1. Schematic illustration of the investigated chip sample. A series of I/S/F/S film samples of length $L = 1.1$ mm along the x axis and width $W = 130\ \mu m$ along the y axis is placed directly on top of the central line of superconducting CPW (in the illustration, only one such film structure is shown). Magnetic field H is applied in-plane along the x axis, and the rf magnetic field H_{rf} oscillates along the y axis (shown with black arrows). The orange arrow beside $\vec{m}$ indicates resonant precession of magnetization in the S/F/S subsystem. The blue curve with blue arrows beside $\vec{b}$ indicates the magnetic field component of the Swihart electromagnetic standing wave in the S/I/S subsystem. The g term indicates the photon-to-magnon coupling.
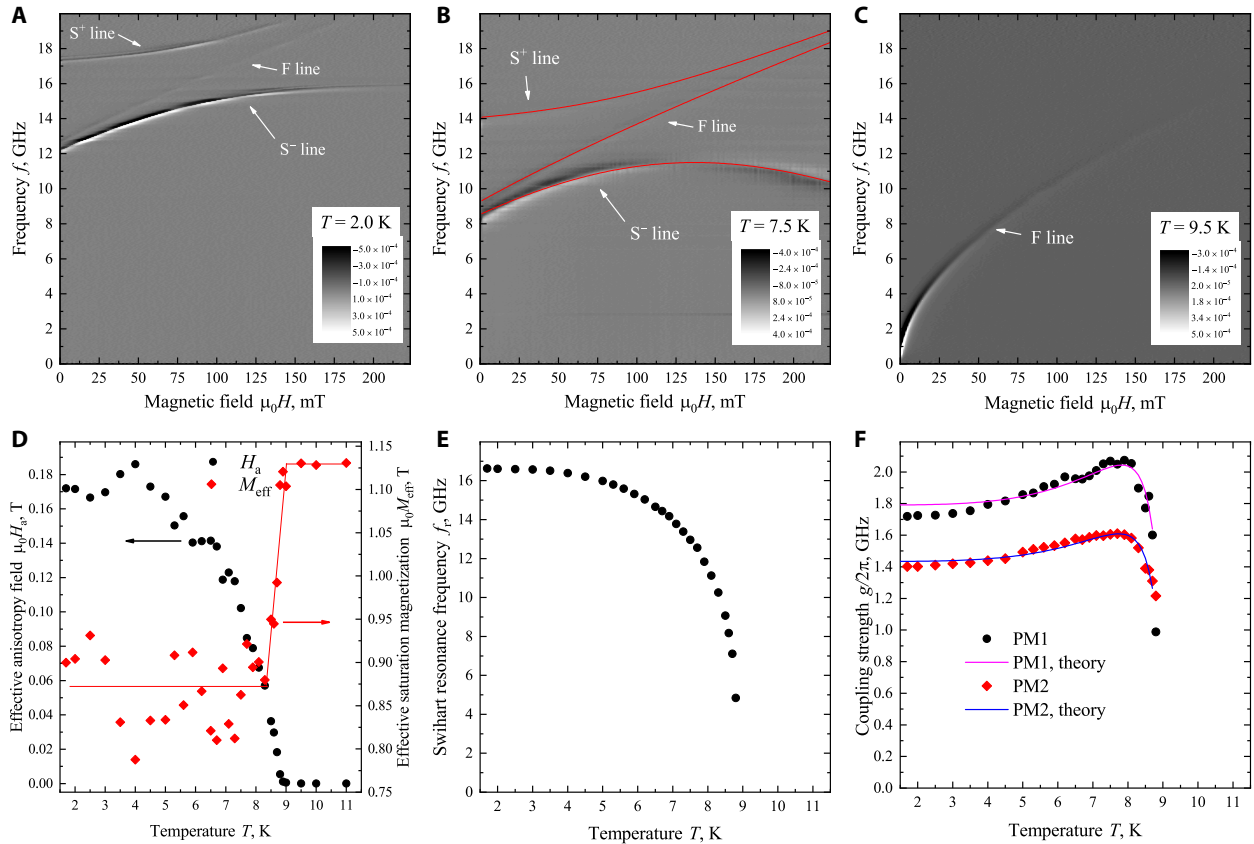
Fig. 2. Microwave response and resonance properties of the hybrid magnonic system. (A to **C)** Microwave transmission spectra $d\,|S_{21}|\,(f, H)/dH$ of the PM1 sample measured at different temperatures below (A and B) and above (C) the superconducting critical temperature. Red curves in (B) show modeling of spectral lines with Eqs. 1, 3, and 4 at the corresponding temperature. **(D)** Temperature dependencies of the proximity-induced anisotropy $H_a(T)$ and effective magnetization $M_{eff}(T)$ of the ferromagnetic S/F/S subsystem (see Eq. 1). The red line in (D) is provided as an eye guide for $M_{eff}(T)$. **(E)** Temperature dependence of the zero-field Swihart resonance frequency f_r^{S0} (T) of the S/I/S subsystem (see Eq. 3). **(F)** Temperature dependence of the coupling strength $g(T)/2\pi$ between S/F/S and S/I/S subsystems for the PM1 sample and also for the supplementary PM2 sample (see Eq. 4). Solid lines in (F) show the fit with the model Eq. 5. The optimum fit with Eq. 5 yields the zero-temperature London penetration depth in the S/F/S multilayer $\lambda_0 = 77.9$ nm and $\alpha = 228.6$ GHz nm$^{3/4}$ for the PM1 sample, and $\lambda_0 = 80.0$ nm and $\alpha = 180.0$ GHz nm$^{3/4}$ for the PM2 sample.

on the thickness of the superconducting film (*38*), which transforms $\lambda_L \propto H^2$ to $\lambda_L \propto H^4$. At this stage, the model for the Swihart resonance frequency $f_r^S(T, H)$ can be proposed by introducing field dependence of λ_L in Eq. 2

$$f_r^S(T,H) = f_r^{S0}(T)/\sqrt{1 + \alpha_1(T)H^2 + \alpha_2(T)H^4} \qquad (3)$$

where $f_r^{S0}(T) = \bar{c}(T, H = 0)/2L$ is the temperature-dependent zero-field Swihart resonance frequency and $\alpha_1(T)$ and $\alpha_2(T)$ are free temperature-dependent parameters.

In summary, transmission spectra in Fig. 2 (A and B) show the FMR absorption in the S/F/S subsystem, which follows the Kittel field dependence (Eq. 1) and the collective response of two harmonic oscillators indicated as S$^+$ and S$^-$ lines: the ferromagnetic S/F/S resonator and the Swihart S/I/S resonator (Eq. 3). The coupling between the S/F/S and S/I/S resonators is schematically depicted in Fig. 1. When two harmonic oscillators are coupled, their resonance spectrum is represented by the anti-crossing, with the coupling strength g being half of the minimum split between spectral lines. For instance, from Fig. 2 (A and B), it follows that $2g/2\pi > 3$ GHz at $T = 2$ K, and $2g/2\pi \approx 4$ GHz at $T = 7.5$ K. For the PM1 sample, the

ratio of the coupling strength to the Swihart resonance frequency is $g/2\pi f_r^S \approx 0.1$ at 2 K and increases substantially at higher temperatures. This value indicates that the hybrid system operates well in the ultrastrong coupling regime (*15*, *39*) of the light-matter interaction where the conventional interaction model (*13*, *14*, *35*) fails. The most general model of the light-matter interaction, the Hopfield model (*39*, *40*), which includes the counter-rotating interaction terms and also the demagnetizing term (*41*), provides the following biquadratic expression (*40*) for anti-crossing spectral lines (see section S2 for details)

$$f_r^{+(-)4} - f_r^{+(-)2}\left(f_r^{S2} + f_r^{F2} + 4\left(\frac{g}{2\pi}\right)^2\right) + f_r^{S2}f_r^{F2} = 0 \qquad (4)$$

Equations 1, 3, and 4 are used for quantitative analysis of microwave transmission spectra at different temperatures using the following routine. First, the F line is fitted separately at each temperature with Eq. 1. The fit yields temperature-dependent proximity-induced anisotropy $H_a(T)$ and effective magnetization $M_{eff}(T)$ shown in Fig. 2D. Both $H_a(T)$ and $M_{eff}(T)$ are well consistent with proximity-induced anisotropies in S/F/S systems (*27*). Next, S$^+$ and S$^-$ lines are fitted with Eq. 4 using $H_a(T)$ and $M_{eff}(T)$ as fixed parameters and using parameters of the Swihart resonator (Eq. 3) and the coupling

strength as fitting parameters. Examples of modeling of resonance lines of the PM1 sample with Eqs. 1, 3, and 4 are given in Fig. 2B and section S3. The optimum fit yields the temperature-dependent zero-field Swihart resonance frequency $f_r^{S0}(T)$ and the coupling strength $g(T)/2\pi$ given in Fig. 2 (E and F, respectively). Zero-field Swihart resonance frequency $f_r^{S0}(T)$ decreases with temperature reaching zero at $T = T_c$ owing to the temperature dependence of the London penetration depth $f_r^{S0}(T) \propto 1/\sqrt{\lambda_L(T)} \propto [1 - (T/T_c)^4]^{1/4}$. A more advanced analysis of the spectrum can be performed with the input-output theory [see, for instance, (14, 19, 20, 35, 42)], which provides the decay rates of resonators in addition to the resonance frequencies and the coupling. However, rather weak signals and the presence of background resonances do not allow us to attempt such analysis in this work.

The high value of the coupling strength and its dependence on temperature $g(T)/2\pi$ are the key achievements of this work. The curve $g(T)/2\pi$ in Fig. 2F is nonmonotonous: Upon increasing temperature, it grows progressively from about 1.72 GHz up to a peak value of 2.07 GHz at $T = 7.9$ K and then decreases rapidly while approaching the critical temperature. The achieved peak coupling strength is a high value as compared to other photon-to-magnon hybrids, exceeding the coupling strength in typical cavity-based (9, 13, 16), split ring–based (43), and on-chip resonator–based (19, 20) hybrids. This coupling strength is comparable only with the coupling in macroscopic photon-to-magnon hybrids (14, 15, 17, 18, 35), where dimensions of the ferromagnetic oscillator reach several millimeters. Along with the total coupling, the system demonstrates a strong single-spin coupling strength (9, 13, 14, 35, 43) $g_s/2\pi = g/2\pi/\sqrt{N} = 88$ Hz at $T = 7.9$ K, where N is the number of spins in the system. This value of $g_s/2\pi$ exceeds ones for cavity-based (9, 13, 14), split ring–based (43), and flip chip–based (35) hybrids by several orders of the magnitude and is only comparable with coupling values achieved recently in on-chip hybrids (19, 20).

All statements above are verified with a supplementary PM2 sample that consists of a similar Swihart resonator and a different-volume ferromagnetic subsystem. Such system is expected to demonstrate different total coupling strength with the same single-spin coupling strength as compared to the PM1 sample. Section S1 collects experimental data for the PM2 sample that consist of I/S/F/S = Si (15 nm)/Nb (110 nm)/Py (19 nm)/Nb (110 nm) rectangles placed on top of a 120-nm-thick Nb waveguide (see Table 1 and Fig. 1). The coupling strength $g(T)/2\pi$ for the PM2 sample is given in Fig. 2F. The curve $g(T)/2\pi$ shows similar temperature dependence with the one for the PM1 sample: The maximum coupling of 1.61 GHz is reached at $T = 7.7$ K. As expected, at the same T, the coupling strength in the PM2 sample is reduced as compared to the PM1 sample, owing to the thinner F layer, while the single-spin coupling strength of the PM2 sample at $T = 7.7$ K $g_s/2\pi = 89$ Hz agrees with the one for the PM1 sample.

As a final remark to this subsection, we analyze the coupling of the Swihart resonators to the transmission line, define two practical characteristics of coupling, and discuss the origin of the F line. Analysis of the complex S_{21} scattering parameters of Swihart resonances (44) provides the loaded quality factor $Q_l \approx 10^2$ and the coupling quality factor $Q_c \approx 10^3 - 10^4 \gg Q_l$. This indicates that the Swihart resonator is coupled weakly to the transmission line as compared to the coupling to the ferromagnetic subsystem. The information exchange rate between the magnon and photon modes during interaction at a specified frequency is represented by the

coupling constant k (43) and is defined as $k = \sqrt{2(g/2\pi)/f_r^S}$. Often, the coupling ratio g/ω_r instead of the coupling constant is used (14, 17, 39). Estimations show that the coupling constant for PM1 and PM2 samples reaches 0.92 (the coupling ratio reaches 0.43), which indicates the ultrastrong coupling regime of the light-matter interaction (39) with one of the highest coupling ratios among hybrid magnonic systems [see (14, 15, 18) for comparison]. Another important practical parameter is the cooperativity C (19, 35) that is defined as $C = (g/2\pi)^2/\Delta f_r^{S^+} \Delta f_r^{S^-}$, where $\Delta f_r^{S^+}$ and $\Delta f_r^{S^-}$ are the linewidth of the S^+ and S^- lines, respectively, taken at magnetic field of the coupling. Cooperativity characterizes coherence between damped oscillators. Insufficient cooperativity leads to suppression of the coherent information exchange between oscillators and to damping of the signal instead of resolved avoided crossing spectrum. Estimations provide the maximum $C = 240$ for the PM1 sample and $C = 109$ for the PM2 sample at 2 K. These values are fairly large as compared to other magnonic hybrids based on metallic ferromagnets (19, 20), offering a great flexibility in circuit integration, although the cooperativity of yttrium iron garnet (YIG) based hybrids (18) is far to be reached (see section S4 for more details).

A distinctive feature that is present at all transmission spectra measured below T_c (see Fig. 2, A and B, and section S1) is the presence of an additional F line. Conventionally, a spectrum of a hybrid system that consists of two coupled harmonic oscillators contains only two anti-crossing lines (13, 14, 16, 20). However, in case of sufficiently strong coupling, the spectrum can incorporate additional lines in the range between the anti-crossing lines that appear as a result of hybridization of higher-order photon or magnon modes (14, 17, 18, 42, 43). Additional studies at temperatures in proximity to T_c do not confirm the presence of higher-order Swihart resonance modes. On the other side, experimental spectra do not contain features that are expected for interaction of the fundamental Swihart resonance mode with the higher-order magnonic modes in the S/F/S multilayer (45, 46). Therefore, the F line in our study is not a signature of hybridization of higher-order modes. The alternative explanation, which is partially supported by supplementary experiments, implies that the F line is a result of FMR absorption by an edge area of ferromagnetic film, which is poorly coupled with the Swihart resonator but is coupled to the transmission line (see section S8 for details).

The fundamental reason for strong photon-to-magnon coupling in studied samples is rather straightforward. The single-spin coupling strength is inversely proportional to the mode volume V_c of electromagnetic resonator $g_s \propto 1/\sqrt{V_c}$ (14, 19, 35). The suppressed photon velocity $\bar{c}$ in the Swihart resonator (Eq. 2) provides a reduced resonance length and small overall dimensions of the resonator. For instance, both the electric mode volume of the PM1 resonator $V_c^{SE} = L \times W \times d_I = 4.3 \times 10^{-15}$ m^3 and its magnetic volume $V_c^{SM} \approx L \times W \times (2\lambda_L + d_I) = 2.8 \times 10^{-14}$ m^3 are well comparable with the volume of the ferromagnetic layer $V^F = L \times W \times d_F = 5.0 \times 10^{-15}$ m^3. Using other terms, high single-spin coupling strength is provided by essentially low impedance Z of the Swihart resonator $g_s \propto 1/\sqrt{Z}$ (20). The impedance of the S/I/S resonator of the PM1 sample at 2 K can be estimated as $= 1/(2\pi f_r^S C) = 0.02$ ohms, where $C = \varepsilon_0 \varepsilon L W/d_I = 4.7 \times 10^{-10}$ F is its capacitance.

Understanding the microscopic mechanism of the coupling is challenging and requires additional experiments provided in section S5. First, one should note that the geometry of the studied structure is essentially the infinite thin-film geometry. The presence

of the photon-to-magnon coupling between S/I/S and S/F/S oscillators is equivalent to the presence of alternating magnetic fields H_y^S induced by the microwave resonator in the F layer (see Fig. 3). Supplementary experiments evidence that the realization of the coupling requires both S layers for the S/F/S subsystem and the presence of the superconducting proximity at both S/F interfaces and excludes conventional magnetostatics as a possible source of the coupling. Combination of these factors implies that the only possibility for the coupling is when the entire S/F/S trilayer acts as a single upper superconducting layer of the Swihart resonator. In other words, the presence of nonzero H_y^S in the F layer is equivalent to the presence of coherent Meissner-like fields and superconducting currents J_x^S in the entire S/F/S trilayer including the F layer as illustrated in Fig. 3.

The suggested mechanism of the coupling obeys the following quantitative model (see section S6)

$$g(T)/2\pi \ = \ \alpha\,\lambda_{\text{eff}}(T)^{-3/4}\sinh\left(\frac{d_S + d_F/2}{\lambda_{\text{eff}}(T)}\right)/\sinh\left(\frac{2\,d_S + d_F}{\lambda_{\text{eff}}(T)}\right) \ (5)$$

where α is a free fitting parameter and $\lambda_{\text{eff}}(T)$ is the effective penetration depth that depends on the London penetration depth at zero temperature λ_0, on T_c, on thicknesses d_S and d_F in the S/F/S multilayer, and on temperature T. Figure 2F shows the experimental and model dependencies of the coupling strength on temperature where the critical temperature T_c = 9.05 K and the cutoff temperature 8.7 K were used. The optimum fit with Eq. 5 yields λ_0 = 77.9 nm for the PM1 sample and λ_0 = 80.0 nm for the PM2 sample. The obtained λ_0 is perfectly consistent with the typical values for sputtered Nb thin films, which verifies the proposed model. According to the model, the increase in coupling strength upon increasing temperature at $T < 8$ K occurs because of the increase in the Meissner field H_y^S in the F layer (the sinh term), while the rapid drop of the coupling at $T > 8$ K occurs because of the simultaneous increase in the mode volume of the resonator and reduction of the resonance frequency (the $\lambda_{\text{eff}}^{-3/4}$ term). The model can be confirmed further by comparing the amplitude of microwave fields oscillating

in the resonator H_{rf} with the typical first critical field in Nb $H_{c1} \approx 100$ mT. Estimations following (20) provide $\mu_0 H_{rf} \approx 1.2$ mT, which is far below H_{c1}, thus securing the Meissner operation regime of microwave resonators (see section S6).

Notice that earlier research studies (25–27) have shown that the presence of superconducting layers at both sides of the F film and the superconducting proximity at both S/F interfaces of an S/F/S layer leads to a substantial increase in the FMR frequency. This phenomenon is also confirmed in the present study. As a possible origin of that phenomenon, it was proposed (25) that the long-range spin-triplet superconducting condensate is formed in the F layer and that spin-polarized spin-triplet Cooper pairs induce additional torque on ferromagnetic moments via the spit-transfer-torque mechanism, which causes the increase in FMR frequency f_r^F. Moreover, the effect of the superconducting triplet pairing on ferromagnetic anisotropies in S/F structures was recently addressed in (47, 48). The current study evidences the presence of superconducting current in the F layer in exactly the same conditions. The large thickness of the considered F films (20 nm and 35 nm) in comparison with the spin-singlet coherence length $\xi_F \approx 1$ nm hints at the spin-triplet origin of registered superconducting coherence. Thus, a set of different research studies points toward the formation of a spin-triplet superconducting condensate in the F layer of the S/F/S trilayers.

In general, only two mechanisms are known for the formation of the spin-triplet superconductivity in S/F/S trilayers. The first one requires the presence of strong spin-orbit coupling at S/F interfaces (29), which can hardly be related to the current study. The second one requires the presence of noncollinear ferromagnetic inhomogeneities F′ at both S/F interfaces as compared to the orientation in F bulk, i.e., the so-called spin-triplet generator S/F′FF′/S structure (29, 31, 49–51). We presume that the latter mechanism can be responsible for the formation of the spin-triplet Cooper pairs in our S/F/S induced by magnetization precession. In proximity to S/F interfaces, the ferromagnetic state is different from the bulk. This state is commonly attributed to additional surface anisotropies induced by surface tensions and by chemical composition at the S/F interface, to enhanced Gilbert damping due to the interface roughness, and to the difference in demagnetizing fields as compared to the bulk of the film. At FMR, any of these effects leads to a reduction in amplitude of magnetization precession for spins at the interface in comparison to the bulk, i.e., to the formation of dynamic noncollinear spin state, as illustrated in Fig. 3B.

In summary, in this work, we demonstrate a new platform for the realization of the ultrastrong photon-to-magnon coupling in on-chip thin-film heterostructures between the superconductor/insulator/superconductor electromagnetic resonator and the superconductor/ferromagnet/superconductor ferromagnetic resonator. High characteristics of coupling are achieved owing to suppressed photon phase velocity in the electromagnetic subsystem. The route for further enhancement of the coupling strength is rather straightforward: One can consider a microwave resonator with even smaller phase velocity that is fabricated using superconducting materials with larger λ_L and dielectric materials with higher ε, paving the way toward deep-strong coupled systems. In addition, magnetic materials with lower losses, including YIG or $Co_{0.25}Fe_{0.75}$, will further enhance cooperativity. Apart from quantum magnonics, the demonstrated platform offers further developments in superconducting Josephson junction–based magnonic systems.
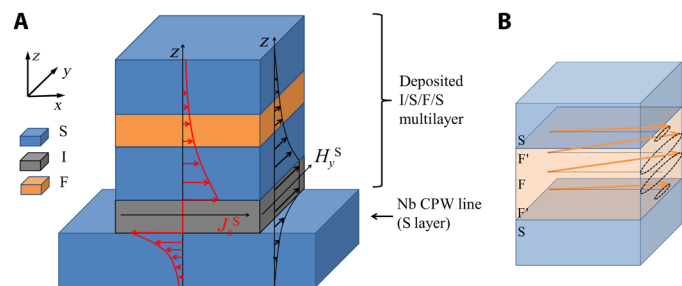

Fig. 3. Microscopic mechanism of the photon-to-magnon coupling. (A) Schematic illustration of field and current distributions that lead to photon-to-magnon coupling. Black curves and arrows indicate the distribution of the magnetic field component $H_y^S(z)$ of the electromagnetic standing wave in superconducting layers of the Swihart resonator. Red arrows with red curves indicate the distribution of superconducting currents $J_x^S(z)$ that support the electromagnetic standing wave in superconducting layers of the Swihart resonator. **(B)** Schematic illustration of the concept of dynamic spin-triplet generator. The amplitude of magnetization precession (orange arrows and dashed circles) is suppressed in proximity to the S/F interface as compared to the bulk of the film. Distribution in the amplitudes forms the dynamic noncollinear F′FF′ spin state.

The microscopic mechanism behind the demonstrated coupling evidences excitation of superconducting coherence in superconductor/ferromagnet/superconductor trilayers via strong thick ferromagnetic layers in the presence of magnetization dynamics. The length scales suggest the spin-triplet origin of superconducting coherence opening new perspectives in the microwave superconducting spintronics.

MATERIALS AND METHODS

A schematic illustration of the investigated hybrid systems is shown in Fig. 1. The system consists of superconducting film CPW and a series of identical multilayered rectangular film heterostructures placed directly on top of the transmission line. The waveguide is fabricated out of the superconducting Nb film deposited on top of the Si/SiO$_x$ substrate using magnetron sputtering of Nb, optical lithography, and plasma-chemical etching techniques; the waveguide has 50-ohm impedance and 82 μm–150 μm–82 μm center-gap-center dimensions. Multilayered film heterostructures are fabricated with lateral dimensions $L \times W = 1100$ μm × 130 μm and spacing in between 200 μm out of superconducting Nb, ferromagnetic permalloy (Py = Fe$_{20}$Ni$_{80}$), and insulating Si or AlO$_x$ layers using optical lithography, magnetron sputtering, and the lift-off techniques. Deposition of these layers is performed in a single vacuum cycle, ensuring electron transparency at all-metallic Nb/Py interfaces. Multilayered heterostructures are fabricated as a series array of 40 identical $L \times W$ rectangles along CPW for the enhancement of total microwave response. A number of different samples have been fabricated and measured with different thicknesses and orders of superconducting (S), ferromagnetic (F), and insulating (I) layers (see Table 1). Microwave spectra for PM1 sample are shown and discussed in this contribution. Microwave spectra for other samples are shown and discussed in supplementary materials.

The experimental chip was installed in a brass sample holder and wire bonded to a printed circuit board with RF connectors. A thermometer and a heater were attached directly to the holder for precise temperature control. The holder was placed in a superconducting solenoid inside a dry closed-cycle He4 cryostat (Oxford Instruments Triton). The response of experimental samples was studied by analyzing the transmitted microwave signal $|S_{21}|(f, H)$ with the VNA Rohde & Schwarz ZVB20. For the removal of background parasitic resonance modes from consideration, all measured spectra $|S_{21}|(f, H)$ have been normalized with $|S_{21}|(f)$ at $\mu_0 H = 0.3$ T and differentiated numerically with respect to H. The response of experimental samples was studied in the field range from −0.22 to

0.22 T, in the frequency range from 0 up to 20 GHz, and in the temperature range from 1.7 to 11 K.

SUPPLEMENTARY MATERIALS

Supplementary material for this article is available at http://advances.sciencemag.org/cgi/content/full/7/25/eabe8638/DC1

REFERENCES AND NOTES

1. F. Flamini, N. Spagnolo, F. Sciarrino, Photonic quantum information processing: A review. *Rep. Prog. Phys.* **82**, 016001 (2019).
2. X. Gu, A. F. Kockum, A. Miranowicz, Y.-x. Liu, F. Nori, Microwave photonics with superconducting quantum circuits. *Phys. Rep.* **718–719**, 1–102 (2017).
3. A. A. Clerk, K. W. Lehnert, P. Bertet, J. R. Petta, Y. Nakamura, Hybrid quantum systems with circuit quantum electrodynamics. *Nat. Phys.* **16**, 257–267 (2020).
4. Z.-L. Xiang, S. Ashhab, J. Q. You, F. Nori, Hybrid quantum circuits: Superconducting circuits interacting with other quantum systems. *Rev. Mod. Phys.* **85**, 623–653 (2013).
5. M. Aspelmeyer, T. J. Kippenberg, F. Marquardt, Cavity optomechanics. *Rev. Mod. Phys.* **86**, 391 (2014).
6. D. Lachance-Quirion, S. P. Wolski, Y. Tabuchi, S. Kono, K. Usamil, Y. Nakamura, Entanglement-based single-shot detection of a single magnon with a superconducting qubit. *Science* **367**, 425–428 (2020).
7. Y. Tabuchi, S. Ishino, A. Noguchi, T. Ishikawa, R. Yamazakia, K. Usami, Y. Nakamura, Quantum magnonics: The magnon meets the superconducting qubit. *C. R. Phys.* **17**, 729–739 (2016).
8. Y. Tabuchi, S. Ishino, A. Noguchi, T. Ishikawa, R. Yamazaki, K. Usami, Y. Nakamura, Coherent coupling between a ferromagnetic magnon and a superconducting qubit. *Science* **349**, 405–408 (2015).
9. D. Lachance-Quirion, Y. Tabuchi, A. Gloppe, K. Usami, Y. Nakamura, Hybrid quantum systems based on magnonics. *Appl. Phys. Exp.* **12**, 070101 (2019).
10. Y.-P. Wang, G.-Q. Zhang, D. Xu, T.-F. Li, S.-Y. Zhu, J. S. Tsai, J. Q. You, Quantum simulation of the fermion-boson composite quasi-particles with a driven qubit-magnon hybrid quantum system. arXiv:1903.12498 (2019).
11. X. Zhang, C.-L. Zou, N. Zhu, F. Marquardt, L. Jiang, H. X. Tang, Magnon dark modes and gradient memory. *Nat. Comm.* **6**, 8914 (2015).
12. R. Hisatomi, A. Osada, Y. Tabuchi, T. Ishikawa, A. Noguchi, R. Yamazaki, K. Usami, Y. Nakamura, Bidirectional conversion between microwave and light via ferromagnetic magnons. *Phys. Rev. B* **93**, 174427 (2016).
13. Y. Tabuchi, S. Ishino, T. Ishikawa, R. Yamazaki, K. Usami, Y. Nakamura, Hybridizing ferromagnetic magnons and microwave photons in the quantum limit. *Phys. Rev. Lett.* **113**, 083603 (2014).
14. X. Zhang, C.-L. Zou, L. Jiang, H. X. Tang, Strongly coupled magnons and cavity microwave photons. *Phys. Rev. Lett.* **113**, 156401 (2014).
15. G. Flower, M. Goryachev, J. Bourhill, M. E. Tobar, Experimental implementations of cavity-magnon systems: From ultra strong coupling to applications in precision measurement. *New J. Phys.* **21**, 095004 (2019).
16. I. Boventer, C. Dorflinger, T. Wolz, R. Macedo, R. Lebrun, M. Klaui, M. Weides, Control of the coupling strength and linewidth of a cavity magnon-polariton. *Phys. Rev. Res.* **2**, 013154 (2020).
17. B. Z. Rameshti, Y. Cao, G. E. W. Bauer, Magnetic spheres in microwave cavities. *Phys. Rev. B* **91**, 214430 (2015).
18. J. Bourhill, N. Kostylev, M. Goryachev, D. L. Creedon, M. E. Tobar, Ultrahigh cooperativity interactions between magnons and resonant photons in a YIG sphere. *Phys. Rev. B* **93**, 144420 (2016).
19. Y. Li, T. Polakovic, Y.-L. Wang, J. Xu, S. Lendinez, Z. Zhang, J. Ding, T. Khaire, H. Saglam, R. Divan, J. Pearson, W.-K. Kwokk, Z. Xiao, V. Novosad, Z. Hoffmann, W. Zhang, Strong coupling between magnons and microwave photons in on-chip ferromagnet-superconductor thin-film devices. *Phys. Rev. Lett.* **123**, 107701 (2019).
20. J. T. Hou, L. Liu, Strong coupling between microwave photons and nanomagnet magnons. *Phys. Rev. Lett.* **123**, 107702 (2019).
21. G. Csaba, A. Papp, W. Porod, Perspectives of using spin waves for computing and signal processing. *Phys. Lett. A* **381**, 1471–1476 (2017).
22. Y. Kajiwara, K. Harii, S. Takahashi, J. Ohe, K. Uchida, M. Mizuguchi, H. Umezawa, H. Kawai, K. Ando, K. Takanashi, S. Maekawa, E. Saitoh, Transmission of electrical signals by spin-wave interconversion in a magnetic insulator. *Nature* **464**, 262–266 (2010).
23. S. Klingler, V. Amin, S. Geprägs, K. Ganzhorn, H. Maier-Flaig, M. Althammer, H. Huebl, R. Gross, R. D. McMichael, M. D. Stiles, S. T. B. Goennenwein, M. Weiler, Spin-torque excitation of perpendicular standing spin waves in coupled YIG/Co heterostructures. *Phys. Rev. Lett.* **120**, 127201 (2018).
24. Y. Li, W. Cao, V. P. Amin, Z. Zhang, J. Gibbons, J. Sklenar, J. Pearson, P. M. Haney, M. D. Stiles, W. E. Bailey, V. Novosad, A. Hoffmann, W. Zhang, Coherent spin pumping

Table 1. IDs and thicknesses of layers in studied samples given in nanometers.

Sample no.	Nb-CPW (S$_1$)	I (Si or AlO$_x$)	S$_2$ (Nb)	F (Py)	I (AlO$_x$)	S$_3$ (Nb)
PM1	140	Si-30	102	35	0	103
PM2	120	Si-15	110	20	0	110
PM3	140	Si-15	110	20	0	5
PM4	140	Si-15	110	20	0	140
PM5	500	AlO$_x$-15	110	25	100	110

in a strongly coupled magnon-magnon hybrid system. *Phys. Rev. Lett.* **124**, 117202 (2020).

25. L.-L. Li, Y.-L. Zhao, X.-X. Zhang, Y. Sun, Possible evidence for spin-transfer torque induced by spin-triplet supercurrents. *Chin. Phys. Lett.* **35**, 077401 (2018).

26. K.-R. Jeon, C. Ciccarelli, H. Kurebayashi, L. F. Cohen, X. Montiel, M. Eschrig, T. Wagner, S. Komori, A. Srivastava, J. W. Robinson, M. G. Blamire, Effect of meissner screening and trapped magnetic flux on magnetization dynamics in thick $Nb/Ni_{80}Fe_{20}/Nb$ trilayers. *Phys. Rev. Appl.* **11**, 014061 (2019).

27. I. A. Golovchanskiy, N. N. Abramov, V. S. Stolyarov, V. I. Chichkov, M. Silaev, I. V. Shchetinin, A. A. Golubov, V. V. Ryazanov, A. V. Ustinov, M. Y. Kupriyanov, Magnetization dynamics in proximity-coupled superconductor-ferromagnet-superconductor multilayers. *Phys. Rev. Appl.* **14**, 024086 (2020).

28. J. Linder, J. W. A. Robinson, Superconducting spintronics. *Nat. Phys.* **1**, 307–315 (2015).

29. M. Eschrig, Spin-polarized supercurrents for spintronics: A review of current progress. *Rep. Prog. Phys.* **78**, 104501 (2015).

30. V. V. Ryazanov, V. A. Oboznov, A. Y. Rusanov, A. V. Veretennikov, A. A. Golubov, J. Aarts, Coupling of two superconductors through a ferromagnet: Evidence for a π junction. *Phys. Rev. Lett.* **86**, 2427–2430 (2001).

31. J. W. A. Robinson, J. D. S. Witt, M. G. Blamire, Controlled injection of spin-triplet supercurrents into a strong ferromagnet. *Science* **329**, 59–61 (2010).

32. T. I. Larkin, V. V. Bol'ginov, V. S. Stolyarov, V. V. Ryazanov, I. V. Vernik, S. K. Tolpygo, O. A. Mukhanov, Ferromagnetic Josephson switching device with high characteristic voltage. *Appl. Phys. Lett.* **100**, 222601 (2012).

33. O. M. Kapran, A. Iovan, T. Golod, V. M. Krasnov, Observation of the dominant spin-triplet supercurrent in Josephson spin valves with strong Ni ferromagnets. *Phys. Rev. Res.* **2**, 013167 (2020).

34. L. Parlato, R. Caruso, A. Vettoliere, R. Satariano, H. G. Ahmad, A. Miano, D. Montemurro, D. Salvoni, G. Ausanio, F. Tafuri, G. P. Pepe, D. Massarotti, C. Granata, Characterization of scalable Josephson memory element containing a strong ferromagnet. *J. Appl. Phys.* **127**, 193901 (2020).

35. H. Huebl, C. W. Zollitsch, J. Lotze, F. Hocke, M. Greifenstein, A. Marx, R. Gross, S. T. B. Goennenwein, High cooperativity in coupled microwave resonator ferrimagnetic insulator hybrids. *Phys. Rev. Lett.* **111**, 127003 (2013).

36. J. C. Swihart, Field solution for a thin-film superconducting strip transmission line. *J. Appl. Phys.* **32**, 461 (1961).

37. T. Hanaguri, Y. Iino, A. Maeda, T. Fukase, Magnetic-field dependence of the London penetration depth in type-II superconductor V_3Si. *Physica C* **246**, 223–227 (1995).

38. A. I. Gubin, K. S. Ilin, S. A. Vitusevich, M. Siegel, N. Klein, Dependence of magnetic penetration depth on the thickness of superconducting Nb thin films. *Phys. Rev. B* **72**, 064503 (2005).

39. A. F. Kockum, A. Miranowicz, S. D. Liberato, S. Savasta, F. Nori, Ultrastrong coupling between light and matter. *Nat. Rev. Phys.* **1**, 19–40 (2019).

40. N. S. Mueller, Y. Okamura, B. G. M. Vieira, S. Juergensen, H. Lange, E. B. Barros, F. Schulz, S. Reich, Deep strong light-matter coupling in plasmonic nanoparticle crystals. *Nature* **583**, 780–784 (2020).

41. P. Nataf, C. Ciuti, No-go theorem for superradiant quantum phase transitions in cavity QED and counter-example in circuit QED. *Nat. Commun.* **1**, 72 (2010).

42. C. Potts, J. Davis, Strong magnon–photon coupling within a tunable cryogenic microwave cavity. *Appl. Phys. Lett.* **116**, 263503 (2020).

43. B. Bhoi, B. Kim, J. Kim, Y.-J. Cho, S.-K. Kim, Robust magnon-photon coupling in a planar-geometry hybrid of inverted split-ring resonator and YIG film. *Sci. Rep.* **7**, 11930 (2017).

44. S. Probst, F. B. Song, P. A. Bushev, A. V. Ustinov, M. Weides, Efficient and robust analysis of complex scattering data under noise in microwave resonators. *rev. sci. inst.* **86**, 024706 (2015).

45. I. A. Golovchanskiy, N. N. Abramov, V. S. Stolyarov, V. V. Bolginov, V. V. Ryazanov, A. A. Golubov, A. V. Ustinov, Ferromagnet/superconductor hybridization for magnonic applications. *Adv. Funct. Mater.* **28**, 1802375 (2018).

46. I. A. Golovchanskiy, N. N. Abramov, V. S. Stolyarov, V. V. Ryazanov, A. A. Golubov, A. V. Ustinov, Modified dispersion law for spin waves coupled to a superconductor. *J. Appl. Phys.* **124**, 233903 (2018b).

47. L. G. Johnsen, N. Banerjee, J. Linder, Magnetization reorientation due to the superconducting transition in heavy-metal heterostructures. *Phys. Rev. B* **99**, 134516 (2019).

48. C. González-Ruano, L. G. Johnsen, D. Caso, C. Tiusan, M. Hehn, N. Banerjee, J. Linder, F. G. Aliev, Superconductivity assisted change of the perpendicular magnetic anisotropy in V/MgO/Fe junctions. arXiv:2006.02118 (2020).

49. F. S. Bergeret, A. F. Volkov, K. B. Efetov, Enhancement of the Josephson current by an exchange field in superconductor-ferromagnet structures. *Phys. Rev. Lett.* **86**, 3140 (2001).

50. M. Houzet, A. I. Buzdin, Long range triplet Josephson effect through a ferromagnetic trilayer. *Phys. Rev. B* **76**, 060504 (2007).

51. T. S. Khaire, M. A. Khasawneh, W. P. Pratt Jr., N. O. Birge, Observation of spin-triplet superconductivity in Co-based Josephson junctions. *Phys. Rev. Lett.* **104**, 137002 (2010).

52. I. A. Golovchanskiy, N. N. Abramov, V. S. Stolyarov, I. V. Shchetinin, P. S. Dzhumaev, A. S. Averkin, S. N. Kozlov, A. A. Golubov, V. V. Ryazanov, A. V. Ustinov, Probing dynamics of micro-magnets with multi-mode superconducting resonator. *J. Appl. Phys.* **123**, 173904 (2018).

53. V. V. Schmidt, *The Physics of Superconductors. Introduction to Fundamentals and Applications*, P. Muller, A. V. Ustinov, Eds. (Springer-Verlag Berlin Heidelberg, 1997).

54. C. Eichler, A. J. Sigillito, S. A. Lyon, J. R. Petta, Electron spin resonance at the level of 10^4 spins using low impedance superconducting resonators. *Phys. Rev. Lett.* **118**, 037701 (2017).

Citation: I. A. Golovchanskiy, N. N. Abramov, V. S. Stolyarov, M. Weides, V. V. Ryazanov, A. A. Golubov, A. V. Ustinov, M. Y. Kupriyanov, Ultrastrong photon-to-magnon coupling in multilayered heterostructures involving superconducting coherence via ferromagnetic layers. *Sci. Adv.* **7**, eabe8638 (2021).

ScienceAdvances

Ultrastrong photon-to-magnon coupling in multilayered heterostructures involving superconducting coherence via ferromagnetic layers

Igor A. Golovchanskiy, Nikolay N. Abramov, Vasily S. Stolyarov, Martin Weides, Valery V. Ryazanov, Alexander A. Golubov, Alexey V. Ustinov and Mikhail Yu. Kupriyanov

ARTICLE TOOLS	http://advances.sciencemag.org/content/7/25/eabe8638
SUPPLEMENTARY MATERIALS	http://advances.sciencemag.org/content/suppl/2021/06/14/7.25.eabe8638.DC1
REFERENCES	This article cites 51 articles, 3 of which you can access for free http://advances.sciencemag.org/content/7/25/eabe8638#BIBL
PERMISSIONS	http://www.sciencemag.org/help/reprints-and-permissions

Use of this article is subject to the Terms of Service